S.T. Yau High School Science Award

Research Report

The Team

Name of team member: Sophie Y. Zheng
School: Rowland Hall
City, Country: Salt Lake City, Utah, USA

Name of supervising teacher: Subo Dong
Job Title: Professor
School/Institution: Kavli Institute for Astronomy and Astrophysics, Peking University
City, Country: Beijing, China

Title of Research Report
Investigating the Origins of Hot Neptunes from Radial Velocity Data

Date

08/18/2023

Investigating the Origins of Hot Neptunes from Radial Velocity Data

Sophie Y. Zheng

Abstract

Hot Neptunes are extrasolar planets that are similar in size to Neptune in our solar system but are much closer to their host star, completing an orbit in 10 days or less. The origin of hot Neptunes is not fully understood. A potential large third body at a distance can lead to the migration of long-period planets to become much closer to the host star, and such a dynamical process helps explain the origin of hot Jupiters. We investigate whether hot Neptunes could share a similar origin by analyzing radial velocity data for a sample of 34 hot Neptune systems. Overall, hot Neptune systems have somewhat lower values of linear trend in the radial velocity than hot Jupiter systems. We then perform a maximum likelihood analysis to constrain the joint distribution of mass and distance of the putative third body. Our results show the overall fraction of hot Neptune systems with third bodies to be consistent with unity, higher than 73% at the 2σ level. On average, the third bodies for hot Neptune systems tend to be lower in mass and closer to the stars than those for hot Jupiter systems. This study suggests that hot Neptune systems share the same migration mechanism as hot Jupiters, e.g., through the gravitational effect of third bodies.

Keywords: exoplanets: evolution, migration, dynamics -- radial velocity -- Chi-squared statistic -- Kolmogorov-Smirinov test -- maximum likelihood

Acknowledgement

Sophie Y. Zheng constructed the hot Neptune sample, collected radial velocity (RV) data from literature, performed the model fitting to RV data, wrote codes to perform statistical analyses and create all plots, and wrote the research report.

Subo Dong introduced the research background, provided guidance to the analysis, discussed the results, and gave feedback on the report.

Commitments on Academic Honesty and Integrity

We hereby declare that we

1. are fully committed to the principle of honesty, integrity and fair play throughout the competition.
2. actually perform the research work ourselves and thus truly understand the content of the work.
3. observe the common standard of academic integrity adopted by most journals and degree theses.
4. have declared all the assistance and contribution we have received from any personnel, agency, institution, etc. for the research work.
5. undertake to avoid getting in touch with assessment panel members in a way that may lead to direct or indirect conflict of interest.
6. undertake to avoid any interaction with assessment panel members that would undermine the neutrality of the panel member and fairness of the assessment process.
7. observe the safety regulations of the laboratory(ies) where we conduct the experiment(s), if applicable.
8. observe all rules and regulations of the competition.
9. agree that the decision of YHSA is final in all matters related to the competition.

We understand and agree that failure to honour the above commitments may lead to disqualification from the competition and/or removal of reward, if applicable; that any unethical deeds, if found, will be disclosed to the school principal of team member(s) and relevant parties if deemed necessary; and that the decision of YHSA is final and no appeal will be accepted.

(Signatures of full team below)

x Sophie Zheng

Name of team member: Sophie Y. Zheng

x Subo Dong

Name of supervising teacher: Subo Dong

Table of Contents

1. INTRODUCTION

Observations of extrasolar planets have revealed a variety of populations and enabled statistical studies to learn about their formation and evolution (e.g., Zhu & Dong 2021). Hot Neptunes are extrasolar planets that are similar in size (about 2–6 Earth radii) to Neptune in our solar system but are much closer to their star, completing an orbit in 10 days or less (Dong et al. 2018), in comparison to 165 years for our Neptune. The origin of hot Neptunes is not fully understood. In this work, we aim to investigate the origins of hot Neptunes based on radial velocity data.

Hot Neptunes share remarkable similarities with hot Jupiters. Both populations more likely reside in metal-rich stars and in systems with single-transiting planets (Dong et al. 2018). For the origin of hot Jupiters (see a review by Dawson & Johnson 2018), one theory suggests that the gravity of a massive third outer body brings a long-period Jupiter onto an orbit of high eccentricity (e.g., through the Lidov-Kozai mechanism; Lidov 1962; Kozai 1962) and the subsequent tidal dissipation leads to an orbit much closer to the star.

The first-order effect caused by the acceleration introduced by the putative third body would show up as a linear trend in the long-term radial velocity variation of the planet system. Studying the linear trend in radial velocity data of hot Jupiter systems (e.g., Knutson et al. 2014) and searching for long-period companions (e.g., Bryan et al. 2016) lend support to such a dynamical origin mechanism for hot Jupiters.

Given the similarities between hot Jupiters and hot Neptunes mentioned above, it is natural to ask whether the same dynamical process can also explain the origin of hot Neptunes. The accumulated radial velocity observations over the past decades (e.g., Trifonov et al. 2020) for hot Neptune systems have made such an investigation possible.

In this work, we analyze the radial velocity data for a sample of hot Neptunes, aiming to shed light on the origins of such a population of exoplanets. We present the sample of hot Neptunes, the radial velocity data, and the method in Section 2. In Section 3, based on modeling the radial velocity data, we compare the linear trend distributions of hot Neptune and hot Jupiter systems and constrain the distribution of the potential third bodies. We summarize and discuss our results in Section 4.

2. DATA AND METHOD

We construct a sample of hot Neptunes based on the NASA Exoplanet Archive.[1]

We apply various filters to select hot Neptunes: orbital periods of 10 days or less, size of 2–6 Earth radii, and discovered through transit. The period and radius distribution of the selected planets are shown as blue points in Figure 1.

Next, to constrain the linear trends, the selected systems need to have radial velocity (RV) observations. We search the HARPS RV Bank (Trifonov et al. 2020) and keep only those systems that have radial velocity data in the RV Bank. We end up with 34 hot Neptune systems for our investigation, which are marked as red points in Figure 1. Among them, 12 (22) appear to be single-planet (multiple-planet) systems. For each system, in order to better constrain the linear trend, we further supplement the RV data with those found in literature (as listed in Table 1).

We use `exostriker`[2] to model the available RV data for each system in our sample and constrain the number of planets, the orbital parameters (e.g., semi-major axis, eccentricity, and period), and the linear trend. The initial inputs about planets' orbits are based on values found in literature. The jitter term is included in the error budget to ensure that the best fit has a reduced χ^2 value of unity.

As an example, in Figure 2, we show the RV observation and the model fit for HD285968. The band in the left panel is in fact the sine-like curve with a period of 8.77 days from the best-fit model. The phase-dependent RV variation can be seen in the right panel, where the RV data is folded with the hot Neptune's orbital period of 8.77 days. In the left panel, a clear slope is seen in the bestfit RV curve. With RV data covering a base line of ∼10 years, the linear trend for this system is detected with high significance, $(-2.57 \pm 0.80) \times 10^{-3}\mathrm{m}^{-1}\mathrm{s}^{-1}\mathrm{d}^{-1}$.

Figure 3 shows the RV fitting results for GJ1265, with observational data also covering a baseline of about 10 years. This system is posed as an example of no significant detection of the linear trend, $(-3.4 \pm 3.9) \times 10^{-4}\mathrm{m}^{-1}\mathrm{s}^{-1}\mathrm{d}^{-1}$.

HD1461 is a system with two known planets, and its RV fitting results are plotted in Figure 4. From the RV data, the two planets, with one being the hot Neptune, are clearly detected. With observation covering a baseline of ∼5000 days, the quadratic trend in the RV data is detected.

[1] https://exoplanetarchive.ipac.caltech.edu/
[2] https://github.com/3fon3fonov/exostriker

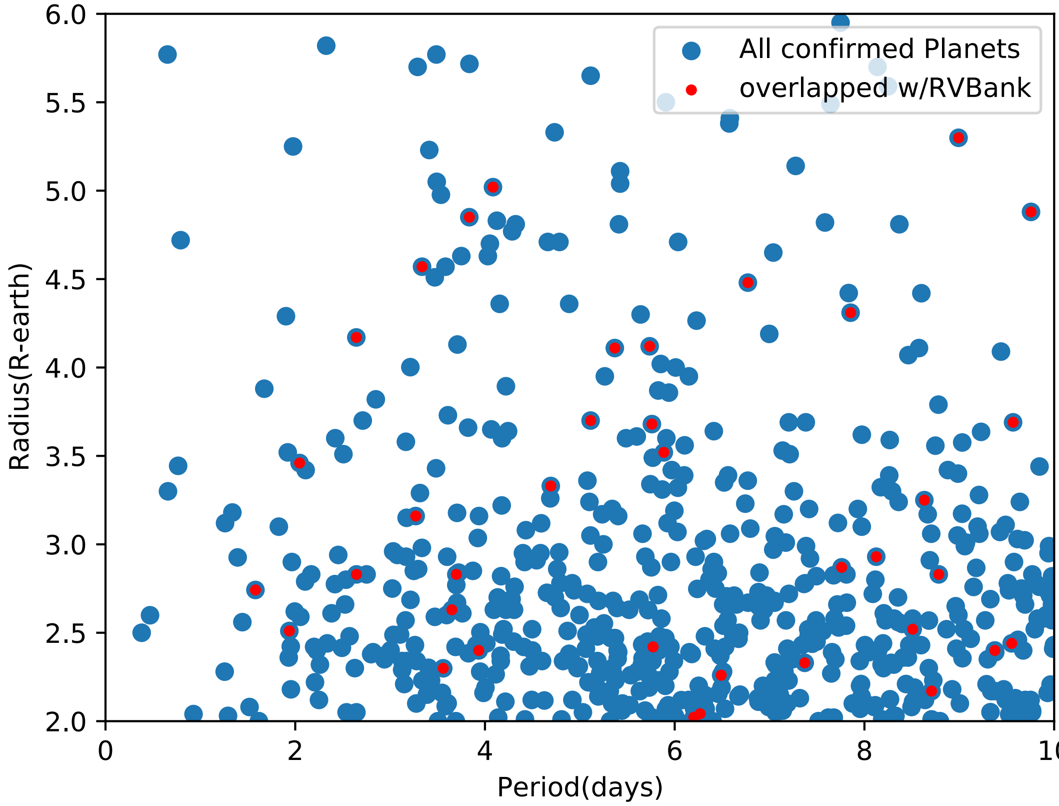

Figure 1. Distribution of hot Neptunes as a function of orbital period and planet radius. The blue dots represent all the hot Neptunes selected from the Exoplanet Archive, while the red dots represent those with enough radial velocity data (the sample in this work).

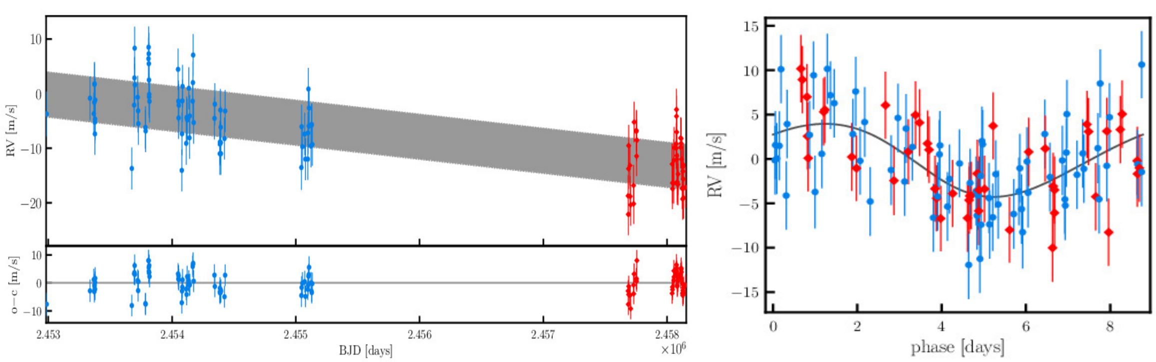

Figure 2. Radial velocity of HD285968. Left: Two sets of radial velocity observations (blue and red data points) with the bestfit model (gray), and the bottom panel shows the residual from the model fit. A significant linear trend is detected for this system. Right: folded RV data within the planet's orbital period.

In Table 1, the linear trend constraints for the 34 hot Neptune systems are listed. To derive the constraints, the model only includes RV trend to the linear order. We

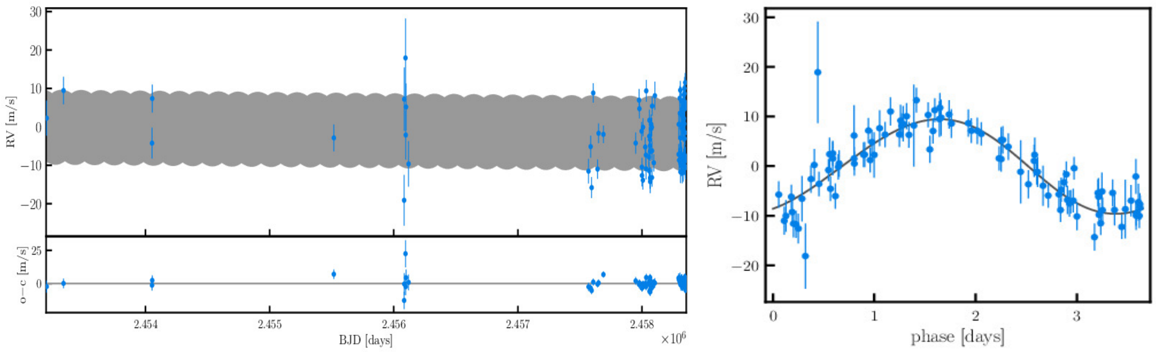

Figure 3. Similar to Figure 2, but for GJ1265. This system does not show a significant linear trend.

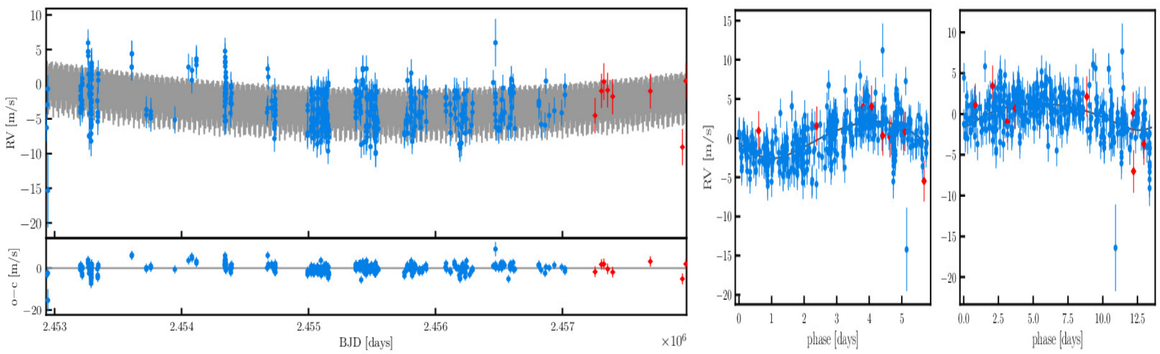

Figure 4. Similar to Figure 2, but for HD1461, which has a significant quadratic trend detected and has two planets.

then extend the model to include RV trend to the quadratic order. Table 2 lists the RV trend constraints for systems with significant quadratic term.

3. CONSTRAINTS ON THE LINEAR TRENDS AND THE THIRD BODY DISTRIBUTION

With our sample of hot Neptune systems, we first analyze the constraints on the derived linear trends and make comparisons to those for hot Jupiter systems. Then, we perform further analysis of the RV data to study the implications for the distributions of masses and distances of the perturbing objects and make comparisons to those for hot Jupiter systems.

In Figure 5, we show the linear trend constraints as a function of planet mass for hot Neptune systems from this work and for hot Jupiter systems in Knutson et al. (2014). The sign of the linear trend is of no importance for our discussion and is

Table 1. Linear trend constraints from our model fitting to the RV data of hot Neptune systems

Name	linear trend ($10^{-2}\mathrm{m}^{-1}\mathrm{s}^{-1}\mathrm{d}^{-1}$)	N_{planet}	RV data sources
CoRoT-7	24.851 ± 4.414	3	1, 8
CoRoT-22	0.766 ± 0.598	1	1, 2
CoRoT-24	-3.119 ± 0.733	2	1, 5
GJ163	-0.042 ± 0.044	5	1, 18
GJ433	0.448 ± 0.416	3	1
GJ436	-0.103 ± 0.057	1	1
GJ480	-0.607 ± 0.337	1	1
GJ536	-0.065 ± 0.021	1	1
GJ581	0.016 ± 0.019	3	1
GJ674	0.031 ± 0.014	1	1
GJ876	1.077 ± 0.400	4	1, 19
GJ1214	3.732 ± 18.410	1	1, 12
GJ1265	-0.034 ± 0.039	1	1, 15
GJ3470	-0.134 ± 0.137	1	1, 21
GJ3634	2.497 ± 0.078	1	1
GJ9827	-2.091 ± 1.204	3	1, 22
HD1461	-0.085 ± 0.010	2	1, 10, 11
HD10180	0.032 ± 0.012	6	1
HD39091	0.418 ± 0.129	2	1, 4
HD47186	0.472 ± 0.025	2	1, 7
HD77338	-0.075 ± 0.033	1	1, 9
HD96700	-0.028 ± 0.011	3	1
HD106315	0.093 ± 0.114	2	1, 3
HD109271	-0.095 ± 0.041	2	1, 6
HD134060	-0.020 ± 0.015	2	1
HD176986	0.015 ± 0.030	2	1
HD181433	0.391 ± 0.039	3	1, 16
HD215497	-0.026 ± 0.068	2	1
HD219828	-0.013 ± 0.035	2	1, 23
HD285968	-0.257 ± 0.080	1	1, 25
HIP54373	-0.085 ± 0.072	2	1, 14
K2-27	-1.042 ± 0.501	1	1, 20
K2-32	0.075 ± 0.116	4	1, 24
K2-138	10.027 ± 2.417	6	1, 17

Note—reference list: 1. Trifonov et al. (2020); 2. Moutou et al. (2014); 3. Kosiarek et al. (2020); 4. Gandolfi et al. (2018); 5. Alonso et al. (2014); 6. Santos et al. (2016); 7. Bouchy et al. (2009); 8. Haywood et al. (2014); 9. Jenkins et al. (2013); 10. Rivera et al. (2009); 11. Rosenthal et al. (2021); 12. Anglada-Escudé et al. (2013); 13. Feng et al. (2019); 14. Luque et al. (2018); 15. Horner et al. (2019); 16. Lopez et al. (2019); 17. Bonfils et al. (2013); 18. Laughlin et al. (2005); 19. Petigura et al. (2017); 20. Bonfils et al. (2012); 21. Teske et al. (2018); 22. Santos et al. (2016); 23. Lillo-Box et al. (2020); 24. Butler et al. (2009).

Table 2. RV trend constraints for systems with significant quadratic trend

Name	linear trend ($m^{-1}s^{-1}d^{-1}$)	quadratic trend ($m^{-1}s^{-1}d^{-2}$)
CoRoT-24	$(-1.04 \pm 0.18) \times 10^{-1}$	$(5.95 \pm 1.51) \times 10^{-5}$
GJ1214	2.21 ± 0.71	$(-1.72 \pm 0.56) \times 10^{-1}$
HD1461	$(-2.83 \pm 0.33) \times 10^{-3}$	$(5.0 \pm 0.8) \times 10^{-7}$
HD176986	$(4.96 \pm 0.87) \times 10^{-3}$	$(-1.04 \pm 0.17) \times 10^{-6}$
HD181433	$(1.90 \pm 0.11) \times 10^{-2}$	$(-3.76 \pm 0.27) \times 10^{-6}$

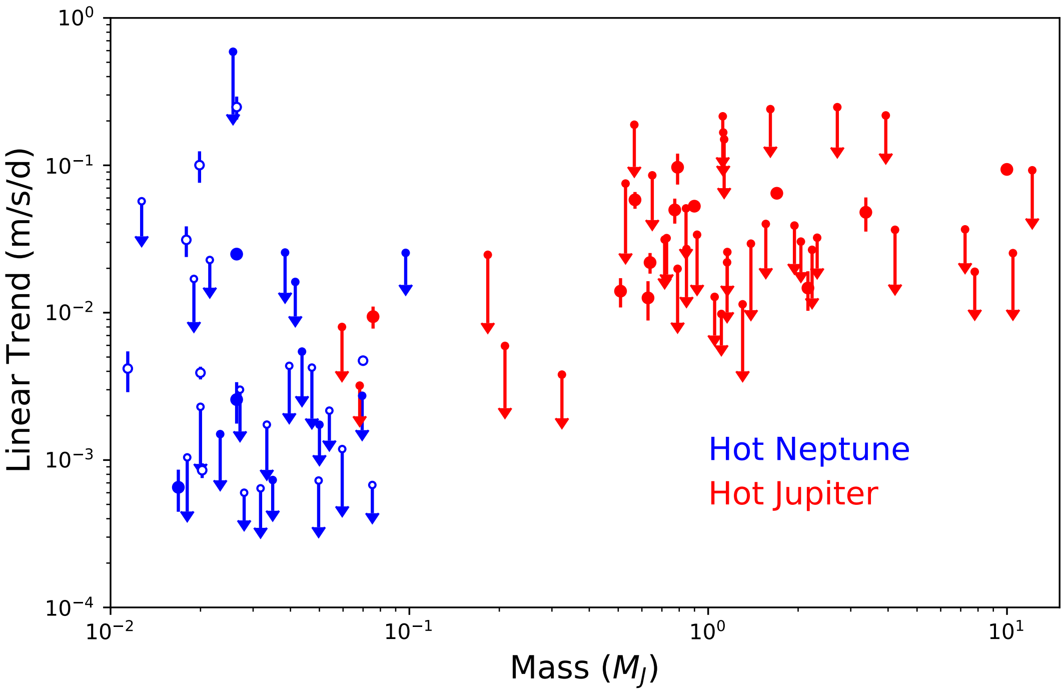

Figure 5. Comparison of linear trends for systems with hot Neptunes (blue) and hot Jupiters (red). The results for hot Neptunes are from this work and those for hot Jupiters are taken from Knutson et al. (2014). Filled and open circles for the hot Neptune systems are for single- and multi-planet systems. Data points with arrows correspond to 3σ upper limits.

neglected. Data points with error bars are for systems with $> 3\sigma$ detection, while arrows show the 3σ upper limit for those without 3σ detection.

Among the 34 hot Neptune systems, 10 systems have linear trend detection, the same fraction as seen in hot Jupiter systems (15 out of 51). However, the distributions of linear trends (including upper limits) of hot Neptune and Jupiter systems appear

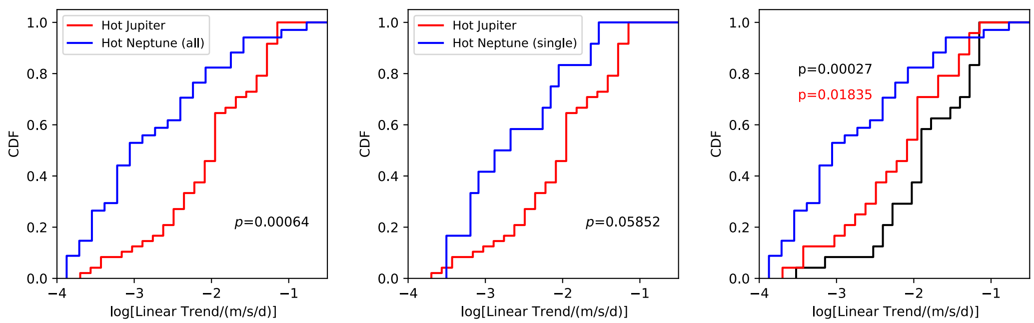

Figure 6. KS tests to compare the distributions of linear trends between hot Neptune and hot Jupiter systems. Left: all hot Neptune systems (blue) versus hot Jupiter systems (red). Middle: single-planet hot Neptune systems (blue) versus hot Jupiter systems (red). Right: all hot Neptune systems (blue) versus high-mass (black) and low-mass (red) hot Jupiter systems . The p value from comparing the distributions is labelled in each panel.

to be different. For hot Jupiter systems, the linear trend constraints are clustered around a few times $10^{-2}\mathrm{m}^{-1}\mathrm{s}^{-1}\mathrm{d}^{-1}$. While some hot Neptune systems have linear trends at such a level, a large faction of them have linear trends about more than one order of magnitude lower, down to a few times $10^{-4}\mathrm{m}^{-1}\mathrm{s}^{-1}\mathrm{d}^{-1}$.

To put the linear trend values into context, we express the expected linear trend caused by a third body of mass m at distance a as

$$\dot{\gamma} = 5.2 \times 10^{-3} \left(\frac{m}{M_J}\right) \left(\frac{a}{10\mathrm{AU}}\right)^{-2} \cos\theta\, \mathrm{m}^{-1}\mathrm{s}^{-1}\mathrm{d}^{-1}, \tag{1}$$

or

$$\dot{\gamma} = 5.2 \times 10^{-2} \left(\frac{m}{M_\odot}\right) \left(\frac{a}{100\mathrm{AU}}\right)^{-2} \cos\theta\, \mathrm{m}^{-1}\mathrm{s}^{-1}\mathrm{d}^{-1}, \tag{2}$$

where θ is the angle between the line connecting the star and the third body and the line of sight. The linear trends hint that the third bodies for hot Neptune systems on average have lower mass and are closer to the stars. The 6 systems with hot Jupiter mass starting to overlap with hot Neptune masses ($\lesssim 0.3M_J$) seem to follow the linear trend constraints seen in the hot Neptune systems.

The comparison hints at a difference in the linear trend distribution between hot Neptune and hot Jupiter systems.

3.1. *KS Tests*

To quantify the potential difference in the distributions, we perform the Kolmogorov–Smirnov (KS) tests. In Figure 6, the left panel compares the cumulative distribution functions (CDFs) of the linear trend constraints for all hot Neptune systems (blue) and hot Jupiter systems (red). The linear trend constraints of hot Neptune systems appear to peak at lower values than those of hot Jupiter systems. The p value is about 0.06%, signaling a significant difference. If we limit hot Neptune systems to single-planet systems (middle panel), the difference remains (p =5.8%).

We further split the hot Jupiter samples into low-mass and high-mass sub-samples by using the median mass $1.1M_J$. The right panel of Figure 6 shows the results. The linear trend distribution of both the low-mass and high-mass hot Jupiter systems (red and black CDFs, respectively) are different from that of hot Neptune systems, but that of the low-mass hot Jupiter systems is less different based on the p values. It is in line with the trend seen in Figure 5 indicated by the 6 hot Jupiter systems with the lowest masses.

One caveat of the above comparisons is that the systems with no significant linear trend detection are taken at the face values of constraints. The p values from the KS tests are not necessarily as meaningful as those from the situation that all systems have stringent linear trend constraints. To reduce such an effect, we perform further KS tests by using the full distribution of the linear trend constraints. In detail, the linear trend constraint of each system is replaced with 10,000 values sampling the constraints (assuming a Gaussian distribution). We find that the trends seen in the comparison results do not change.

Given that a large fraction of hot Neptune and hot Jupiter systems have no significant linear trend detection, the KS tests only serve as a preliminary comparison to provide a crude evaluation of the difference in the linear trend constraints.

3.2. *Maximum Likelihood Analysis of the Third Body Distribution*

To fully account for the cases of both detections and non-detections of linear RV trend, we implement a maximum likelihood method to constrain the mass and distance distributions of the potential third body and compare the results for hot Neptune and hot Jupiter systems.

As the first step, for each hot Neptune system, we add a putative third body to fit the RV data (Wright et al. 2007), together with the existing planet(s). For the i-th hot Neptune system, we find the bestfit χ^2 value, $\chi_i^2(m, a)$, at each location on a grid of semi-major axis a and third body mass $m \sin i$ (assuming zero eccentricity; for simplicity, hereafter we use m for $m \sin i$). Similar to Knutson et al. (2014), we

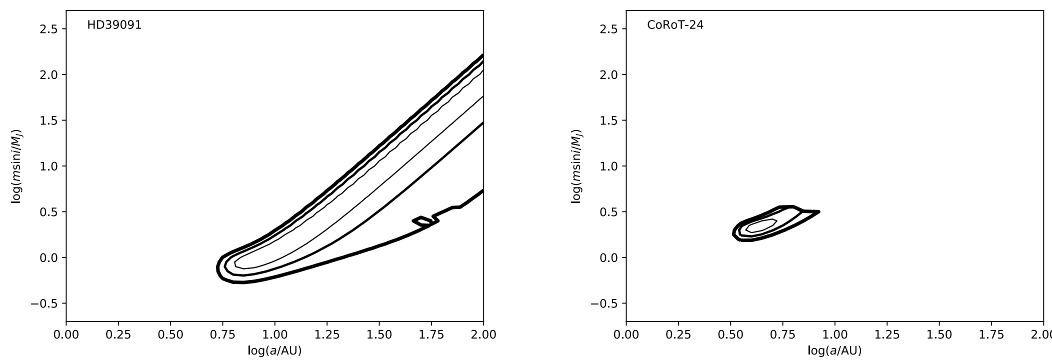

Figure 7. Two examples of constraints on the mass and distance of the putative third body. While for the hot Neptune system in the left panel, the *combination* of mass and distance of the third body is constrained, for the one in the right panel, the mass and distance of the third body are well-constrained. The contours correspond to the 1σ, 2σ, and 3σ confidence levels, respectively.

set the range of m to be 0.2–500M_J and that of a to be 1–100 AU. The likelihood for the third body to have the corresponding m and a is computed as

$$\mathcal{L}_i(m,a) \propto \exp\left\{-[\chi_i^2(m,a) - \chi_i^2]/2\right\}, \tag{3}$$

where χ_i^2 is the minimum of all the $\chi_i^2(m,a)$ values.

The results of the constraints on the mass and distance of the putative third body (a.k.a. Wright plots) for all the systems are shown in the Appendix (Fig. 10). Figure 7 shows two examples. In the first example (HD39091; left panel), the *combination* of mass and distance is constrained. The third body can be a low-mass one closer to the star or a high-mass one farther away from the star. This is largely driven by the fact that the linear trend is proportional to m/a^2, and the RV data does not show significant trend beyond the linear order. For comparison, the RV data in the second example (CoRoT-24; right panel) allows good constraints on the mass and distance of the third body ($\sim 2M_J$ at $\sim$ 4AU).

With the third body's mass and distance constraints for each hot Neptune system, we perform the maximum likelihood analysis to obtain the constraints on the mass and distance distribution of the third body. Following previous work (e.g., Tabachnik & Tremaine 2002; Knutson et al. 2014), we model both the mass (m) and the distance (a) distribution as power law,

$$\frac{d^2P}{d\ln m\, d\ln a} = C m^\alpha a^\beta, \tag{4}$$

where C is the normalization factor. Different from previous work (e.g., Knutson et al. 2014), where C is left free, we fix it for given values of α and β by requiring $\iint Cm^{\alpha}a^{\beta}d\ln m d\ln a = 1$. We then introduce a fraction parameter F to explicitly incorporate the possibility that only a fraction of the systems have a third body. The third-body distribution is then described as $f(m,a) = F \times Cm^{\alpha}a^{\beta}$. By definition, F is the fraction of systems with third bodies and has values between 0 and 1. We consider three sets of hot Neptune systems: the single-planet systems, the multi-planet systems, and the whole sample. For each set of samples, we aim to constrain α, β, and F. Comparisons of the constraints for different samples allow us to tell how different their third body distributions are.

Given the observational data, for each distribution model represented by the model parameters (α, β, F), the probability to have a detection for system i is computed as

$$\mathcal{P}_i(\alpha,\beta,F) = \iint f(m,a|\alpha,\beta,F)p_i(m,a)\,d\ln m\,d\ln a, \tag{5}$$

where $p_i(m,a)$ is the probability in the corresponding ($\ln m$, $\ln a$) cell in the normalized Wright plot, derived based on Equation (3). The probability of non-detection is then $1 - \mathcal{P}_i$. For a given sample, the overall likelihood is (Tabachnik & Tremaine 2002; Knutson et al. 2014)

$$\mathcal{L}(\alpha,\beta,F) = \prod_{i=1}^{N_{\rm d}} \mathcal{P}_i(\alpha,\beta,F) \times \prod_{j=1}^{N_{\rm nd}} \left[1 - \mathcal{P}_j(\alpha,\beta,F)\right], \tag{6}$$

where $N_{\rm d}$ is the number of systems with a significant ($> 3\sigma$) linear trend detection and $N_{\rm nd}$ is that for non-detection.

We obtain parameter constraints by applying the maximum likelihood analysis to all the hot Neptune systems. The marginalized distributions in the α–F and β–F plane are shown in Figure 8. The parameter F, representing the overall fraction of systems with third bodies, is consistent with unity. In fact, the location of the maximum likelihood is at $F = 1$, with $\alpha = -0.56$ and $\beta = 0.22$. The marginalized distribution of F peaks at $F = 1$, and we find F >0.89, >0.73, and >0.55 at the 68.3%, 95.4%, and 99.7% confidence level.

The marginalized distribution of model parameters α and β constrained from all the hot Neptune systems is shown in Figure 9 (blue shaded contours). We find that the

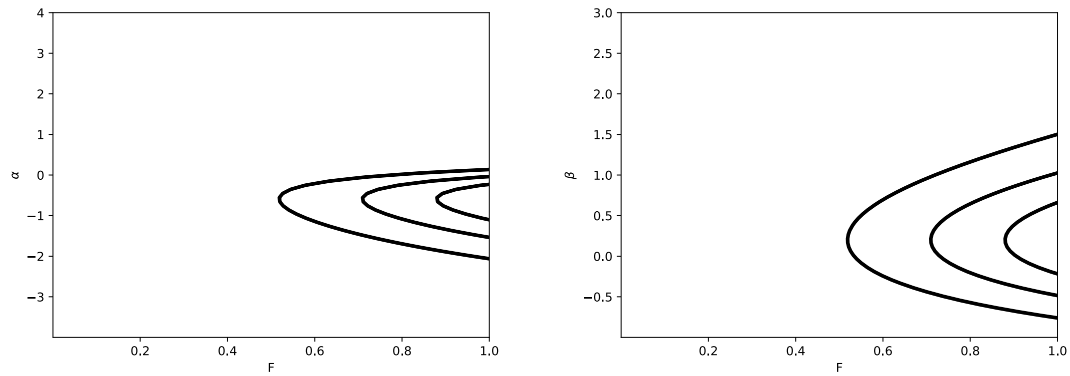

Figure 8. Marginalized distributions the third body mass and distance distribution parameters in the α–F (left) and β–F (right) plane. The parameter F is the overall fraction of hot Neptune systems with third bodies, and α (β) is the power-law index of the mass (distance) distribution function. The contours in each panel correspond to 1σ, 2σ, and 3σ confidence levels.

contours do not vary much if F is fixed to be unity. The 1σ, 2σ, and 3σ constraints for α are (-1.04, -0.44), (-1.46, -0.22), and (-1.98, -0.03), respectively. Those for β are (-0.09, 0.50), (-0.59, 0.87), and (-0.66, 1.35).

If the hot Neptune systems are divided into those of single- and multi-planet systems, the parameter constraints appear to be consistent with each other (see the black and cyan dashed contours).

As a comparison, in Figure 9 we also show the constraints on the third body distribution for hot Jupiter systems (red dashed contours; adopted from Knutson et al. 2014). The 1σ contours for hot Neptune and hot Jupiter systems are well separated. For parameter α, the 2σ ranges of the marginalized distributions for the hot Neptune and hot Jupiter systems are different, (-1.46, -0.22) versus (0.1, 2.3). The lower values of α for hot Neptune systems suggest that the corresponding third bodies on average tend to have lower masses. For parameter β, the hot Neptune systems have slightly lower values, indicating third bodies closer to the host stars. However, the constraints are consistent with those from hot Jupiter systems, e.g., with 1σ ranges of (-0.09, 0.50) versus (0.3, 1.0).

The results from the maximum likelihood analysis qualitatively agree with those indicated by the linear trend distributions and those from the KS tests.

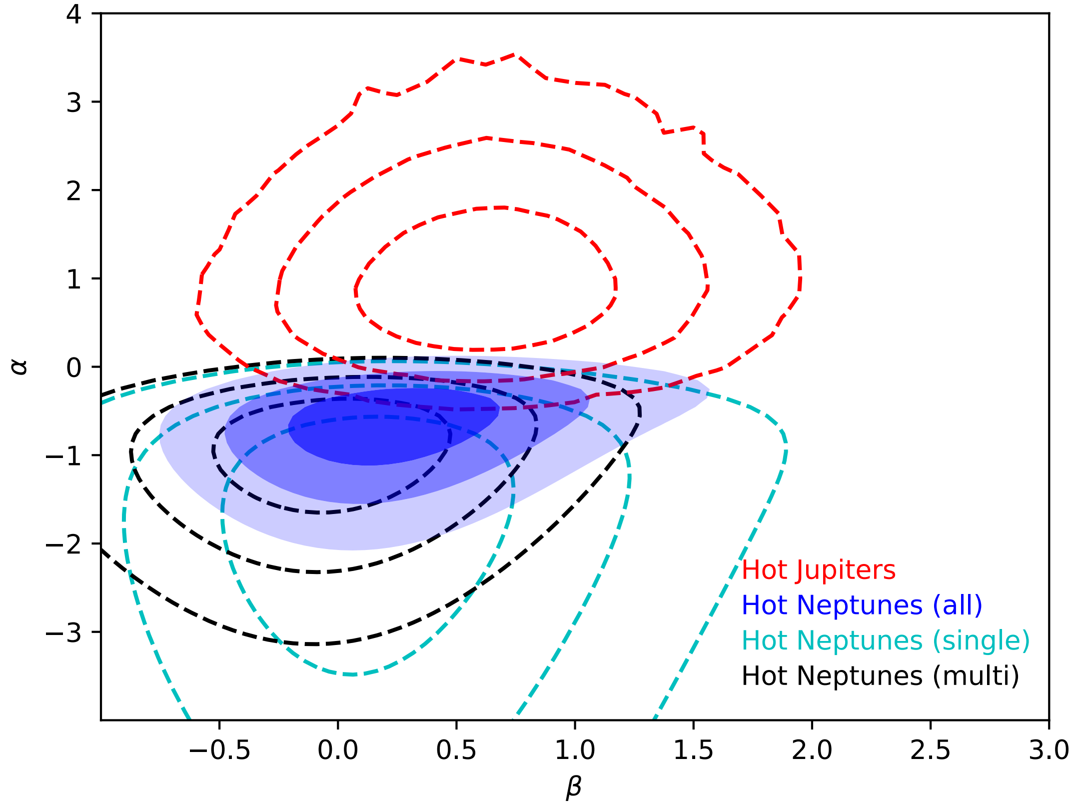

Figure 9. Constraints on the third body mass and distance distribution parameters α and β, where α (β) is the power-law index of the mass (distance) distribution function. The blue shaded contours are constraints for all hot Neptune systems, while the cyan and black dashed contours are for single- and multi-planet hot Neptune systems. For comparison, the constraints of the third body distribution for hot Jupiter systems (red; adopted from Knutson et al. 2014) are overlaid. The contours correspond to 1σ, 2σ, and 3σ confidence levels for two parameters, respectively.

4. SUMMARY AND DISCUSSION

We analyze the linear trends in the radial velocity data of hot Neptune systems and compare their distribution to that of hot Jupiter systems, in order to test the theory about the origin of the hot Neptune systems under the influence of a third body.

For our hot Neptune systems, approximately 30% (10/34) have a significant linear trend, similar to the proportion in hot Jupiter systems (15/51). For single-planet hot Neptune systems, this number is 25% (3/12). The results strongly indicate the existence of external third bodies, supporting the dynamic origins of hot Neptunes.

In detail, the linear trend distribution for all the hot Neptune systems and that for the hot Jupiter systems appear to be different, with the former having more systems with lower linear trends. The above trends are also seen in the results of KS tests using fiducial linear trend constraints. To reduce the effect of non-detection on the KS tests, we employ a maximum likelihood analysis to constrain the mass and distance distribution of the putative third body, which again reveals similar qualitative trends.

The maximum likelihood analysis of the mass and distance distribution of the external third bodies shows that the overall fraction of hot Neptune systems with third bodies is consistent with unity, higher than 73% at a 2σ confidence level. On average, the external bodies for hot Neptune systems are lower in mass than those for hot Jupiter systems and that the difference is at the 2σ level. The third bodies for hot Neptune systems also appear to be closer to host stars than those of hot Jupiter systems, but the difference is not significant.

The constraints suggest that Neptune-like planets, being less massive than Jupiter-like planets, can be more affected by less massive external bodies to migrate to become hot Neptunes.

The constraints on mass and distance of the third bodies of individual hot Neptune systems in this work can guide the search for them, e.g., through imaging observations with adaptive optics (e.g., Bryan et al. 2016). For example, six of the hot Neptune systems (CoRoT-24, GJ536, HD1461, and HD28596, HD77338, and HD181433) are interesting targets for observation, as the distance and mass of the putative third body have been tightly constrained from the RV analysis (see Fig. 10). The observational search for third bodies would provide strong tests on the dynamic origins of hot Neptunes.

With RV observations of more hot Neptune/Jupiter systems and in a longer time span, the constraints on the third bodies are expected to become tighter, which will help further test the origins of these extrasolar planet populations.

APPENDIX

A. CONSTRAINTS ON THE THIRD BODY DISTRIBUTION FOR EACH HOT NEPTUNE SYSTEM

For each hot Neptune system, we fit the RV data by adding a putative body and obtain the constraints (Fig.10) on the mass m and distance a (semi-major axis) of the third body (Wright et al. 2007). The contours correspond to $\Delta\chi^2 = 2.30$, 6.17, and 11.80, to approximate the 1σ, 2σ, and 3σ confidence levels for two parameters. The results are fed to our maximum likelihood analysis.

For CoRoT-7 and GJ9827, the fits do not converge at a large fraction of grid points. These two systems are excluded in our maximum likelihood analysis, although they are put as place holders in Figure 10.

The constraints in most systems show the expected trend of a larger mass at a larger distance. The RV data of several systems allow tighter constraints on the distribution of the third body. For the 5 systems with a significant quadratic trend detection, 3 of them (CoRoT-24, HD1461, and HD181433) have good constraints on the mass and distance of the third body. For systems with good linear trend constraints ($\gtrsim 2\sigma$), some have good third body distribution constraints, such as GJ536, HD77338, and HD285968, while GJ3634 and HD47186 show tight constraints along the m/a^2 degeneracy direction.

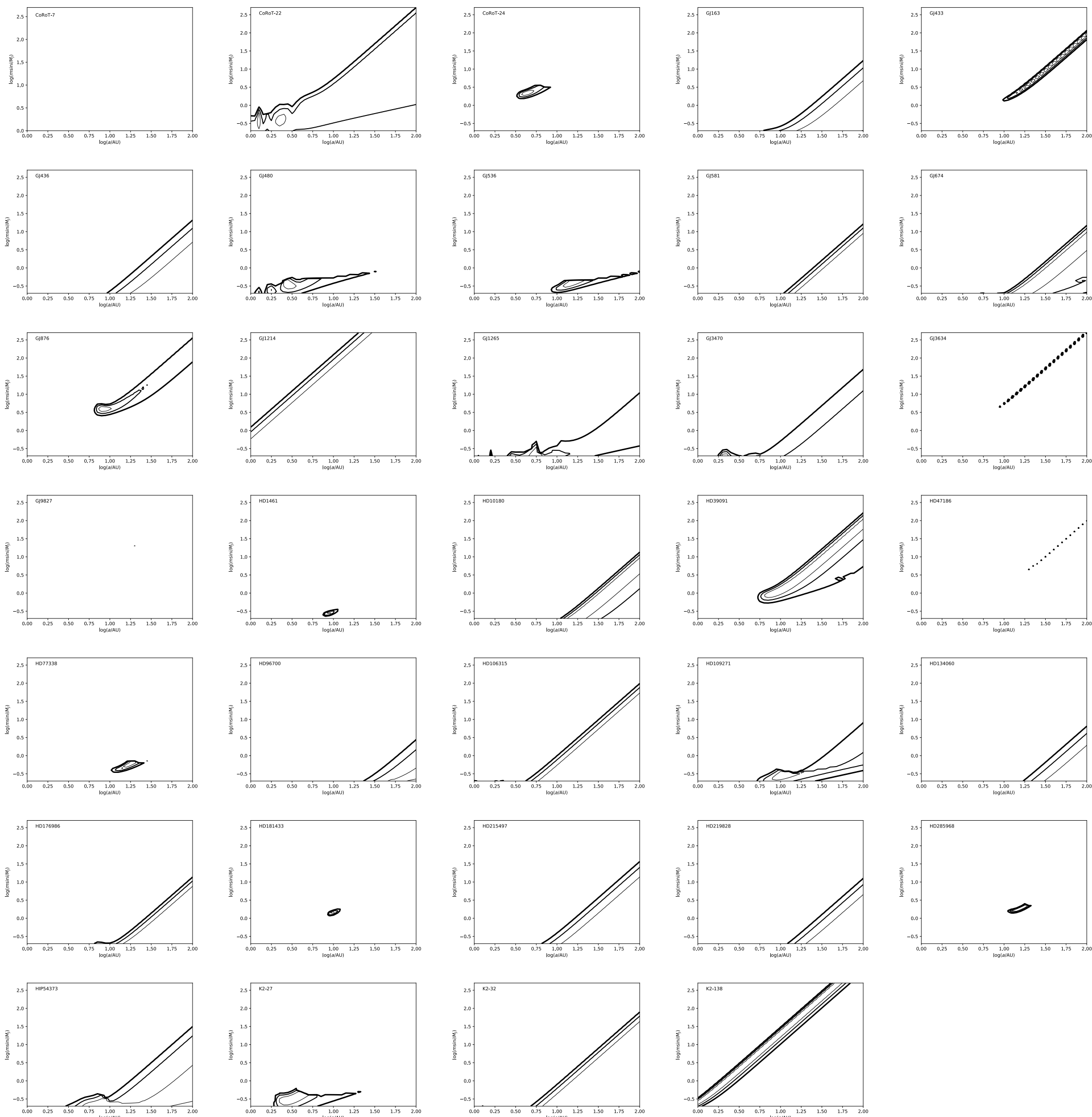

Figure 10. Constraints on the mass and distance distribution of the third body for each hot Neptune system, obtained by adding a putative third body in fitting the RV data. The contours correspond to the 1σ, 2σ, and 3σ confidence levels for two parameters. No converged results are found for CoRoT-7 and GJ9827, and the corresponding panels are put as place holders. See text for more details.

BIBLIOGRAPHY

REFERENCES

Alonso, R., Moutou, C., Endl, M., et al. 2014, A&A, 567, A112,
Anglada-Escudé, G., Rojas-Ayala, B., Boss, A. P., Weinberger, A. J., & Lloyd, J. P. 2013, A&A, 551, A48,
Bonfils, X., Gillon, M., Udry, S., et al. 2012, A&A, 546, A27,
Bonfils, X., Lo Curto, G., Correia, A. C. M., et al. 2013, A&A, 556, A110,
Bouchy, F., Mayor, M., Lovis, C., et al. 2009, A&A, 496, 527,
Bryan, M. L., Knutson, H. A., Howard, A. W., et al. 2016, ApJ, 821, 89,
Butler, R. P., Howard, A. W., Vogt, S. S., & Wright, J. T. 2009, ApJ, 691, 1738,
Dawson, R. I., & Johnson, J. A. 2018, ARA&A, 56, 175,
Dong, S., Xie, J.-W., Zhou, J.-L., Zheng, Z., & Luo, A. 2018, PNAS, 115, 266,
Feng, F., Crane, J. D., Wang, S. X., et al. 2019, ApJS, 242, 25,
Gandolfi, D., Barragán, O., Livingston, J. H., et al. 2018, A&A, 619, L10,
Haywood, R. D., Collier Cameron, A., Queloz, D., et al. 2014, MNRAS, 443, 2517,
Horner, J., Wittenmyer, R. A., Wright, D. J., et al. 2019, AJ, 158, 100,
Jenkins, J. S., Jones, H. R. A., Tuomi, M., et al. 2013, ApJ, 766, 67,
Knutson, H. A., Fulton, B. J., Montet, B. T., et al. 2014, ApJ, 785, 126,
Kosiarek, M. R., Berardo, D. A., Crossfield, I. J. M., et al. 2020, AJ, 161, 47,
Kozai, Y. 1962, AJ, 67, 591,
Laughlin, G., Butler, R. P., Fischer, D. A., et al. 2005, ApJ, 622, 1182,
Lidov, M. L. 1962, Planet. Space Sci., 9, 719,
Lillo-Box, J., Lopez, T. A., Santerne, A., et al. 2020, A&A, 640, A48,
Lopez, T. A., Barros, S. C. C., Santerne, A., et al. 2019, A&A, 631, A90,
Luque, R., Nowak, G., Pallé, E., et al. 2018, A&A, 620, A171,
Moutou, C., Almenara, J. M., Díaz, R. F., et al. 2014, MNRAS, 444, 2783,
Petigura, E. A., Sinukoff, E., Lopez, E. D., et al. 2017, AJ, 153, 142,
Rivera, E. J., Butler, R. P., Vogt, S. S., et al. 2009, ApJ, 708, 1492,
Rosenthal, L. J., Fulton, B. J., Hirsch, L. A., et al. 2021, ApJS, 255, 8,
Santos, N. C., Santerne, A., Faria, J. P., et al. 2016, A&A, 592, A13,
Tabachnik, S., & Tremaine, S. 2002, MNRAS, 335, 151,
Teske, J. K., Wang, S., Wolfgang, A., et al. 2018, AJ, 155, 148,
Trifonov, T., Tal-Or, L., Zechmeister, M., et al. 2020, A&A, 636, A74,
Wright, J. T., Marcy, G. W., Fischer, D. A., et al. 2007, ApJ, 657, 533,
Zhu, W., & Dong, S. 2021, ARA&A, 59, 291,

Declaration of Academic Integrity

The participating team declares that the paper submitted is comprised of original research and results obtained under the guidance of the instructor. To the team's best knowledge, the paper does not contain research results, published or not, from a person who is not a team member, except for the content listed in the references and the acknowledgment. If there is any misinformation, we are willing to take all the related responsibilities.

Names of team members

Sophie Y. Zheng

Signatures of team members

Sophie Zheng

Name of the instructor

Subo Dong

Signature of the instructor

Subo Dong

Date

Aug 18, 2023